Sulfur-induced electron redistribution of single molybdenum atoms promotes nitrogen electroreduction to ammonia

Lu Li [a],[1], Weikang Yu [a],[1], Wenbin Gong [b],[1], Hao Wang [c],[*],[1], Chao-Lung Chiang [d], Yanping Lin [b], Jie Zhao [a], Labao Zhang [c],[*], Jong-Min Lee [e],[*], Guifu Zou [a],[*]

[a] Soochow Institute for Energy and Materials Innovations & Key Laboratory of Advanced Carbon Materials and Wearable Energy Technologies of Jiangsu Province, Soochow University, Suzhou 215006, China
[b] School of Physics and Energy, Xuzhou University of Technology, Xuzhou 221018, China
[c] Research Institute of Superconductor Electronics, School of Electronic Science and Engineering, Nanjing University, Nanjing 210023, China
[d] National Synchrotron Radiation Research Center, Hsinchu 30076, Taiwan, ROC
[e] School of Chemical and Biomedical Engineering, Nanyang Technological University, Singapore, 637459 Singapore

ARTICLE INFO

ABSTRACT

Electrochemical nitrogen reduction reaction (NRR) is considered a sustainable approach that endows NH_3 production from N_2 and H_2O under ambient conditions. Due to the sluggish adsorption/activation of N_2 and the strong competition with the hydrogen evolution reaction, advanced NRR electrocatalysts with both high activity and selectivity are required. Herein, we demonstrate a local modulation strategy that simultaneously promotes NRR selectivity and activity on molybdenum-based single atom catalysts (SACs) by sulfur-induced electronic redistribution, delivering a NH_3 yield rate of 46.6 $\mu g \cdot h^{-1} \cdot mg_{cat.}^{-1}$ and a Faradaic efficiency of 28.9% at a potential of − 0.2 V vs. RHE in 0.1 M HCl under ambient conditions. This study provides a promising strategy for synergizing the selectivity and activity of electrocatalysts toward multistep NRR. Moreover, such an atomic-level engineering strategy should be applicable to other SACs in general and may have a major impact on their use in electrocatalytic applications.

1. Introduction

Ammonia (NH_3), usually generated from naturally abundant nitrogen, is one of the most important chemicals for agriculture and energy fields [1]. Compared with the cumbersome and energy-consuming Haber-Bosch process, electrochemical nitrogen reduction reaction (NRR) can be easily integrated with renewable energy (e.g., solar) and is regarded as an eco-friendly method to achieve sustainable NH_3 production under environmental conditions [2]. Nevertheless, current NRR electrocatalysts usually suffer from poor selectivity and activity, resulting in limited Faradaic efficiency (FE) and NH_3 yield rate [3]. These restrictions mainly arise from two aspects: 1) the low energy barrier for hydrogen adsorption on the surface of the catalyst is favorable for the hydrogen evolution reaction (HER) instead of NRR, causing poor selectivity [4]; 2) the activation and breaking of the N≡N triple bond requires high energy (bond energy of 940.95 kJ mol^{-1}), resulting in poor activity [5]. To overcome these challenges, there is an urgent

need to develop an electrocatalyst with intrinsic activity to suppress the traditionally favorable hydrogen adsorption for NRR.

Single-atom catalysts (SACs), with their maximum atom efficiency and unique electronic properties [6], are attracting tremendous attention and exhibit promising performance toward NRR [7–13]. Among them, molybdenum (Mo)-based SACs with unoccupied d orbitals, which can accept electrons from N_2 and reinforce N_2 adsorption, have been most widely investigated in both theory and experiments [8,14–17]. For instance, Xin et al. [8] reported that the optimal Mo-SACs anchored on nitrogen-doped carbon frameworks had an average yield rate of 34 μg h^{-1} mg$_{cat.}^{-1}$ with an FE of 14.6%. Despite the inspiring computational results, these efforts remain far from providing high selectivity and activity simultaneously for NRR on Mo-SACs. Previous studies have revealed that N-doped carbon-supported Mo-SACs exhibit extremely low hydrogen adsorption free energy (0.082 eV), which is beneficial to HER and thus reduces the selectivity to NRR [18]. Therefore, it is imperative to modulate the electron distribution of Mo-SACs to weaken hydrogen

---

* Corresponding authors.
  E-mail addresses: wanghao91@nju.edu.cn (H. Wang), Lzhang@nju.edu.cn (L. Zhang), jmlee@ntu.edu.sg (J.-M. Lee), zouguifu@suda.edu.cn (G. Zou).
[1] These authors contributed equally

adsorption and facilitate NRR kinetics.

Herein, we report an efficient strategy to optimize the NRR activity of Mo-SACs by modulating the electron distribution with sulfur incorporation. S-doped Mo single atoms/carbon multichannel fibers (Mo_{SA}/CMF-S) are readily obtained by the template-assisted electrospinning method, in which the doped S atoms induce the electron redistribution of isolated Mo atom sites, resulting in enhanced N_2 adsorption and suppressed HER activity. Meanwhile, the designed hierarchical multichannel structure endows the full accessibility of the active site to the electrolyte and facilitates charge transfer during the electrochemical reaction. Consequently, the designed Mo_{SA}/CMF-S exhibits a yield rate of 46.6 $\mu g \cdot h^{-1} \cdot mg_{cat}^{-1}$ with FE of 28.9% at − 0.2 vs. RHE in 0.1 M HCl electrolyte.

2. Experimental section

2.1. Material synthesis

S-doped Mo single atoms/carbon multichannel fibers (Mo_{SA}/CMF-S) was prepared by an electrospun and annealing method. Typically, 0.6 g of Polyacrylonitrile (PAN), 0.8 g of polymethyl methacrylate (PMMA), and 30 mg of ammonium tetrathiomolybdate (ATTM) were dissolved in 10 mL of N,N-dimethylformamide (DMF), which formed a homogeneous solution after 2-hour stirring at 50 °C. During electrospinning, the applied voltage was 20 kV, and the distance between the spinneret and the receiver was 25 cm. By electrospinning under a voltage of 20 kV, a fiber film was obtained, which was then dried at 60 °C overnight. The dried precursor was preoxidized in air at 260 °C for 2 h, followed by annealing in argon at 800 °C for 1 h, and finally Mo_{SA}/CMF-S was obtained. For comparison, carbon multichannel fiber-supported Mo single atoms (Mo_{SA}/CMF) were also prepared with the same method by replacing ATTM with ammonium molybdate. Moreover, the multichannel structure was optimized by adjusting the content ratios of PAN and PMMA. Pure CMF was derived from the precursor consisting of PAN and PMMA.

2.2. Electrochemical measurements

Electrochemical tests were performed in an H-type cell with a three-electrode system in 0.1 M HCl electrolyte solution, where the environment was room temperature and atmospheric pressure. Typically, Ag/AgCl and Pt (1 cm × 1 cm) were used as reference and counter electrode, respectively. In order to eliminate the interference of pollutants, the ion exchange membrane needed to be boiled in DI water and soaked in H_2O_2 (5%) solution at 80 °C, respectively. To prepare the catalyst ink, 2 mg of the prepared catalyst was added to a mixed solution containing 900 μL of ethanol and 100 μL of Nafion solution, and sonicated for 1 h to obtain a homogeneous solution. Subsequently, take 100 μL of the above solution and drop it on the carbon paper (1 cm × 1 cm) and let it air dry naturally to serve as a working electrode. Finally, the electrolyte was purged with high-purity nitrogen (99.999%) for 30 min before each test to remove air and obtain a nitrogen-saturated solution. And the Chronoamperometry tests were performed in a nitrogen-saturated solution for 2 h.

2.3. Simulation

The DFT calculations were performed by using the Vienna ab initio Simulation Package (VASP). The Kohn-Sham wave functions were expanded in a plane wave basis set with a cutoff energy of 500 eV. The projector-augmented wave (PAW) method and PBE potential for the exchange-correlation functional were used. A graphene supercell with a surface periodicity of 6 × 6 was employed as a basis to construct the electrocatalysts, whose Brillouin zone was sampled by a 4 × 4 × 1 k-point mesh. All atoms were allowed to relax until the forces fell below 0.01 eV $Å^{-1}$. A vacuum region of 20 Å perpendicular to the graphene

surface was created to ensure negligible interaction between mirror images. The free energy in this study was calculated following the equation: $\Delta G = \Delta E + \Delta ZPE − T\Delta S$, where ΔG is the reaction free energy, ΔE is the adsorption energy, ΔZPE and $T\Delta S$ are the zero-point energy correction and entropic correction, respectively. All the free energies in this study were obtained by DFT calculation and the standard thermodynamic data for gas molecules. So, the temperature considered in the theoretical analysis was set to be 298 K.

More experimental details can be seen in Supporting Information.

3. Results and discussion

3.1. Preparation and characterization of Mo_{SA}/CMF-S

The synthesis strategy of Mo_{SA}/CMF-S is schematically illustrated in Fig. 1a. Briefly, Mo_{SA}/CMF-S was prepared by carbonizing electrospun precursor nanofibers consisting of polyacrylonitrile (PAN), polymethyl methacrylate (PMMA) and ammonium tetrathiomolybdate. The contrast experiments suggest that a sample with a weight ratio of 20:1 between PAN and ammonium molybdate, defined as Mo-CF-20, endows isolated dispersion of Mo atoms (Fig. S1-S3). Accordingly, S-doped Mo-CF-20 can be easily obtained by replacing ammonium molybdate with ammonium tetrathiomolybdate, which exhibits a monoatomic Mo distribution as well (Fig. S4). On the other hand, PMMA plays a key role in forming the multichannel structure, which forms a multicore structure in the PAN fiber during the electrospinning process [19]. The fibers with a weight ratio of 1:1.3 between PAN and PMMA exhibited the best multichannel structure (Fig. S5). Therefore, a weight ratio of 20:26:1 between the PAN, PMMA and Mo sources was adopted to prepare various Mo-SAC samples. The precursor solutions and derived fiber films are shown in Fig. S6.

The structural properties of the obtained Mo_{SA}/CMF-S, Mo_{SA}/CMF and CMF samples were determined by X-ray diffraction (XRD). The broad diffraction peaks at 23.4° and 43.6° are indexed to the (002) and (101) planes of graphite, respectively (Fig. S7) [20]. Remarkably, no signals related to Mo (e.g., Mo_2C, MoN, MoS_2, etc.) can be observed in these XRD patterns, which means that the Mo atoms in the carbon matrix are highly dispersed [21,22]. Raman spectroscopy also confirmed the atomic dispersion of Mo (Fig. S8). In Mo_{SA}/CMF-S and Mo_{SA}/CMF, except for the existence of carbon characteristics (D and G bands) as CMFs, no signal from metallic Mo and Mo-based compounds is detected in the Raman spectra, suggesting that the isolated Mo atoms are stable without agglomeration or recrystallization in the carbon matrix during high-temperature annealing. Additionally, the intensity ratios of the D and G bands for Mo_{SA}/CMF-S and Mo_{SA}/CMF are 1.09 and 1.03, respectively, indicating that the introduction of S into the single atom sample can induce more disordered carbon and structural defects, which may contribute to mote active sites for electrochemical reactions [23–25]. Rationally, the XRD and Raman results provide evidence for the atomic dispersion of Mo on the carbon support.

The microstructure of Mo_{SA}/CMF-S was studied by electron microscopy techniques. The SEM images (Fig. S9) display the interconnected fibrous morphology of Mo_{SA}/CMF-S with an average diameter of ~300 nm and a multichannel structure. As shown in Fig. 1b, Mo_{SA}/CMF-S has a long hollow multichannel inner hole along the length of the fiber, which can be confirmed by the HAADF-STEM image (Fig. 1c). The corresponding energy dispersive X-ray spectroscopy (EDS) images (Fig. 1d) show that C, N, S and Mo elements are homogeneously distributed in the whole carbon fiber. As shown in Fig. 1e, the enlarged TEM image of the fiber edge reveals its porous structure without metal clusters or particles, suggesting that the Mo atoms should be isolatedly anchored on the carbon matrix. Moreover, the HRTEM image and SAED pattern demonstrate the amorphous characteristic of Mo_{SA}/CMF-S (Fig. S10). Nanocrystals or nanoclusters with a size of less than 1 nm are difficult to observe with common TEM, which indicates that the Mo atoms exist as isolated single atoms. For this reason, aberration-
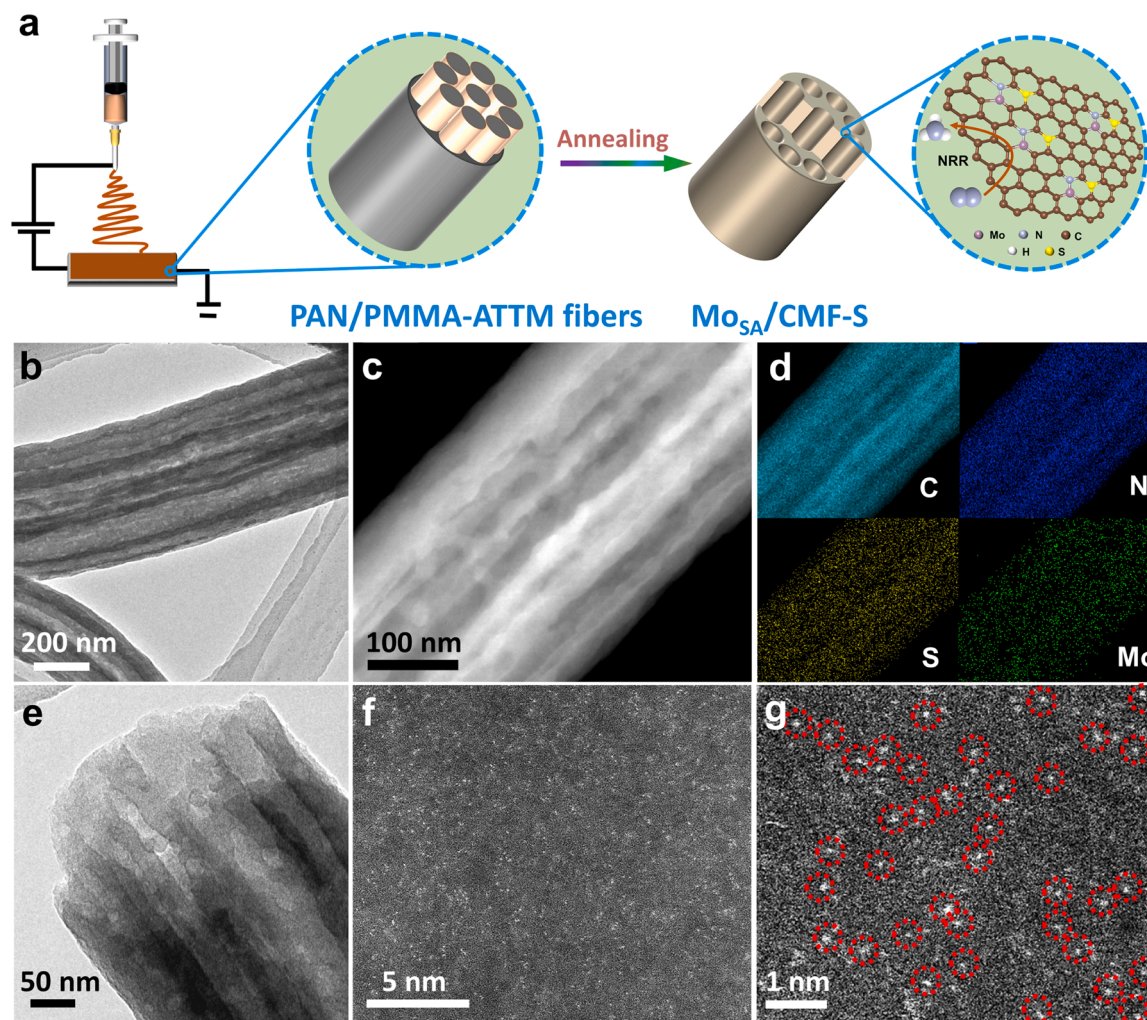
Fig. 1. Synthesis and characterization of Mo$_{SA}$/CMF-S. (a) Schematic illustration of the procedures for preparing S-doped Mo single atoms/carbon multichannel fibers (Mo$_{SA}$/CMF-S). (b) TEM, (c) HAADF-STEM, and (d) corresponding element mapping images of Mo$_{SA}$/CMF-S. (e) Enlarged TEM image focused on the edge of Mo$_{SA}$/CMF-S. (f) Aberration-corrected HAADF-STEM and (g) magnified images of Mo$_{SA}$/CMF-S with highlighting the bright dots by red circles.

corrected HAADF-STEM is conducted to determine the truth. As shown in Fig. 1f, numerous small bright dots are uniformly distributed on the carbon support. The enlarged image (Fig. 1g) highlights these bright dots with red circles, which are identified as single Mo atoms. In addition, the EDX spectrum corresponding to the region in Fig. 1g shows a weak but obvious signal referring to Mo (Fig. S11), further confirming the formation of single Mo sites. This interconnected multichannel porous structure is very conducive to the accessibility of atomic sites and charge transfer in electrochemical processes. To further determine the effect of S on the electrocatalytic performance, Mo$_{SA}$/CMF was also prepared by using ammonium molybdate instead of ammonium tetra-thiomolybdate through a similar method. Dedicated characterizations (Fig. S12) were conducted to identify the multichannel morphology and atomic dispersion properties. According to inductively coupled plasma atomic emission spectroscopy measurements, the Mo contents in Mo$_{SA}$/CMF-S and Mo$_{SA}$/CMF were 0.83 wt% and 0.78 wt%, respectively.

The structure and valence information of Mo$_{SA}$/CMF-S, Mo$_{SA}$/CMF and CMF were analyzed by X-ray photoelectron spectroscopy (XPS). The full XPS spectra (Fig. 2a) show the C, N and O elements in all samples except Mo element is not in the CMF and S element is not in the Mo$_{SA}$-CMFs. The high-resolution Mo 3d spectra can be deconvoluted into four peaks located at 228.74, 231.63, 231.79 and 234.69 eV, referring to Mo^{4+} 3d$_{5/2}$, Mo^{6+} 3d$_{5/2}$, Mo^{4+} 3d$_{3/2}$, and Mo^{6+} 3d$_{3/2}$, respectively (Fig. 2b). The valence states of Mo in both Mo$_{SA}$/CMF and Mo$_{SA}$/CMF-S

are mainly Mo^{4+} and Mo^{6+} (Table S1). There are no Mo clusters (Mo^0) in the samples, further proving that they exist as single-atom isolated states [26]. Notably, the binding energies of Mo 3d for Mo$_{SA}$/CMF-S (Mo^{4+} 3d$_{5/2}$ at 228.74 eV) are negative in comparison with Mo$_{SA}$/CMF (Mo^{4+} 3d$_{5/2}$ at 229.51 eV), indicating an increase in charge density and negative charge [27]. Due to the difference of the electronegativity between different non-metal atoms, when doping S atoms in the single atom sample, the low electronegativity of the S atoms can modulate the coordination environment and thus redistribute the electron density around the isolated Mo atoms [28]. In the high-resolution N 1 s spectra (Fig. 2c), four characteristic peaks at 398.4, 399.8, 401.1 and 403.2 eV are found in all three samples, which represent pyridinic N, pyrrolic N, graphitic N and oxidized N, respectively [29]. The peak at 396.1 eV corresponding to N-Mo bond [30] exists in both Mo$_{SA}$/CMF and Mo$_{SA}$/CMF-S. Compared to CMFs (Table S2), the increase in the N-Mo proportion and the decrease in pyridinic-N content suggest that pyridinic-N provides coordination sites for Mo atoms to form Mo-N$_x$ species [31]. Additionally, for the C 1 s spectrum, the peak at 283.9 eV corresponding to C–Mo bond exists in both Mo$_{SA}$/CMF and Mo$_{SA}$/CMF-S, suggesting the significant electronic coupling at the interfaces between Mo atoms and the carbon matrix (Fig. S13a and S13c) [8]. Meanwhile, there is no O–Mo bond for Mo$_{SA}$/CMF and Mo$_{SA}$/CMF-S in the O 1 s spectrum (Fig. S13b and S13d). Specifically, the integrated peak area associated with N–Mo and C–Mo is determined to be
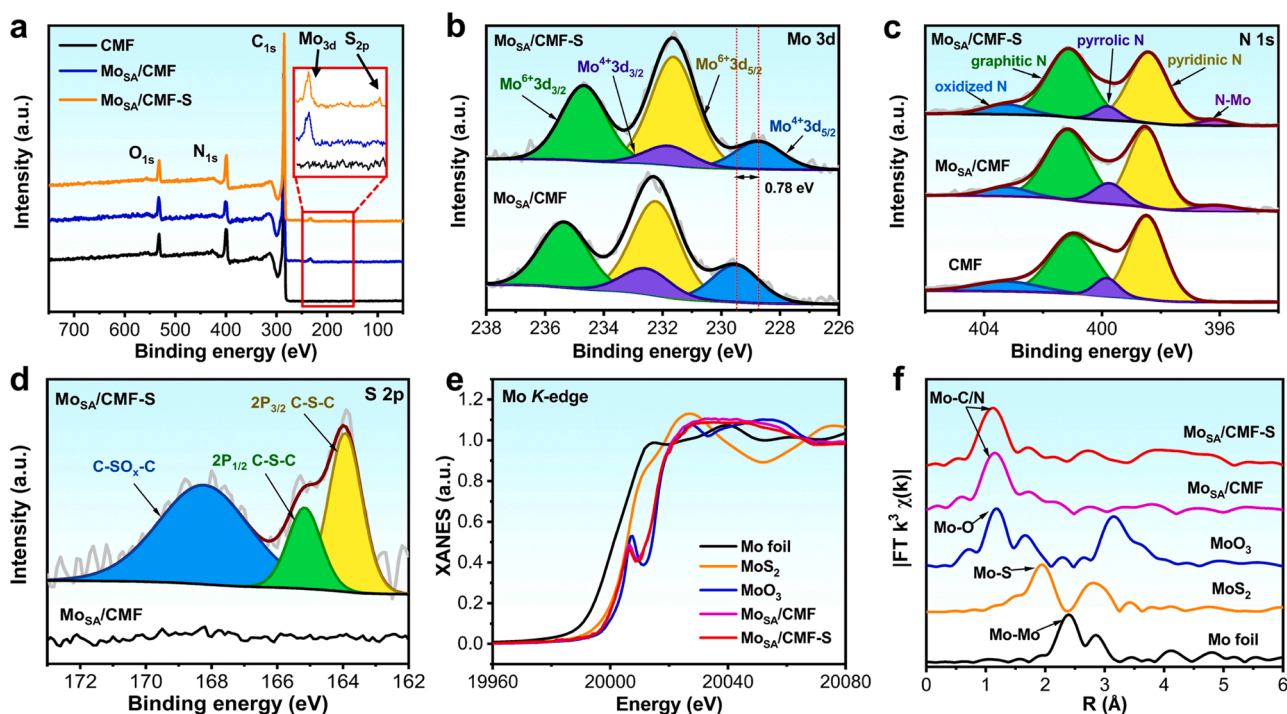
Fig. 2. Composition and atomic coordination investigation by X-ray spectroscopy. (a) XPS full scan of Mo_{SA}/CMF-S, Mo_{SA}/CMF and CMF. High-resolution plots for (b) Mo 3d, (c) N 1 s and (d) S 2p. (e) Mo K-edge XANES and (f) FT-EXAFS spectra of Mo_{SA}/CMF-S, Mo_{SA}/CMF, Mo foil, MoS_2 and MoO_3.

approximately 1:2 (Table S2 and S3), indicating that the Mo atom in Mo_{SA}/CMF and Mo_{SA}/CMF-S is bonded to C and N. The three peaks in the high-resolution S 2p spectrum for Mo_{SA}/CMF-S are attributed to C-S-C (163.9 eV for S $2p_{3/2}$, 165.2 eV for S $2p_{1/2}$, 55.3%) and C-SO$_x$-C (168.2 eV, 44.7%), respectively, suggesting that S is doped into the carbon matrix (Fig. 2d and Table S3) [32] Noted that the C-SO$_x$-C groups can improve the conductivity of carbon matrix, which may facilitate the charge transfer during NRR process [33].

The atomic structure of the Mo coordination environment in Mo_{SA}/CMF-S was analyzed by X-ray absorption spectroscopy. Fig. 2e shows the Mo K-edge X-ray absorption near-edge structure (XANES) of Mo_{SA}/CMF-S and Mo_{SA}/CMF, with Mo foil, MoS_2 and MoO_3 as references. The Mo K-edge of Mo_{SA}/CMF-S is between those of MoS_2 and MoO_3, which can be fitted into two valence states of + 4 and + 6 [34]. This result is consistent with the above XPS analysis. The Fourier transform k^3-weighted extended X-ray absorption fine structure (FT-EXAFS) spectra of Mo_{SA}/CMF-S and Mo_{SA}/CMF have a dominant peak at ~1.12 Å associated with Mo-N/C coordination [8], which indicates that the Mo atoms in Mo_{SA}/CMF-S and Mo_{SA}/CMF are bonded with C or N (Fig. 2f). Additionally, the Mo-Mo contribution is negligible in comparison with the Mo-N/C peak, confirming the isolated dispersion of Mo atoms. This result is in good agreement with Fig. 1g and Fig. S12f. In contrast, the Mo foil shows a typical Mo-Mo pair at 2.39 Å, while the Mo-O interaction of MoO_3 is located at approximately 1.18 Å. Notably, no obvious Mo-S signal can be found in Mo_{SA}/CMF-S compared to Mo_{SA}/CMF, suggesting that S atoms are incorporated into the carbon matrix instead of coordinated with Mo atoms. Based on the EXAFS fitting, the atomically dispersed Mo atoms of Mo_{SA}/CMF-S are anchored on the interconnected multichannel carbon framework with a triple coordination of one N atom and two C atoms ($Mo_1N_1C_2$) (Fig. S14 and Table S4). Therefore, the Mo atoms are coordinated with C/N atoms, and the S atoms are doped into the carbon matrix.

3.2. Electrocatalytic nitrogen reduction performance

The electrochemical NRR performance of Mo_{SA}/CMF-S was

evaluated in an H-type cell with a three-electrode system (Fig. S15). The linear sweep voltammetry curves (Fig. S16a) show that Mo_{SA}/CMF-S provides a higher current density in N_2-saturated 0.1 M HCl solution than that in Ar saturation, indicating that our catalyst is more active as N_2 exists [35]. Specifically, the red curve leads the black curve by a larger margin at − 0.2 V vs. RHE than at − 0.3 V vs. RHE, with a significant ratio of 0.269–0.218 (Fig. S16b). Additionally, under the conditions of Ar and N_2, an onset cathodic current associated with hydrogen evolution appears at − 0 V vs. RHE [36]. Chronoamperometry at different potentials from 0 to − 0.5 V vs. RHE (Fig. S17a) shows that the current densities increase with the applied potential, which is consistent with the LSV curve. The amount of generated NH_4^+ and possible byproduction N_2H_4 can be determined by the calibrated indophenol blue method and Watt-Chrisp method, respectively (for standard calibration details, see Fig. S18 and S19) [37,38]. No peaks regarding N_2H_4 can be detected under the applied potentials, suggesting that Mo_{SA}/CMF-S has excellent selectivity for NH_3 (Fig. S20). The results of UV-Vis absorption of the electrolyte after staining with indophenol indicator for 2 h (Fig. S17b) confirm that NH_3 is indeed produced through NRR catalyzed by Mo_{SA}/CMF-S at a potential from 0 to − 0.5 V vs. RHE. Fig. 3a displays the average NH_3 yield rates and the corresponding FE profiles of Mo_{SA}/CMF-S under different applied potentials. The highest NH_3 yield rate and FE both reach maximum values of 46.6 $\mu g \cdot h^{-1} \cdot mg_{cat}^{-1}$ and 28.9%, at − 0.2 V vs. RHE, respectively, which is higher than that under alkaline and neutral conditions (Fig. S21). After that, the NH_3 yield rate and FE decrease as the potential increases, resulting from the competitive HER process due to the easier proton reduction on active sites [21,39]. As shown in Fig. 3b, the Mo_{SA}/CMF-S catalyst exhibits an NH_3 yield rate of up to 5.61 $mg \cdot h^{-1} \cdot mg_{Mo}^{-1}$ with an FE of 28.9% at − 0.2 V vs. RHE, significantly exceeding those reported for single-atom catalysts [8,9,12,13,40–46] (for more comparison, see Table S5), e.g., SA-Mo/NPC (3.56 mg h^{-1} mg$_{Mo}^{-1}$/14.6%@−0.3 V) [8], SA Ru-Mo_2CT_X (2.88 mg·h^{-1}·mg$_{Ru}^{-1}$/25.7%@−0.3 V) [9], NC-Cu SA (0.93 mg·h^{-1}·mg$_{Cu}^{-1}$/11.7%@−0.3 V) [13] and Fe$_{SA}$-NO-C (4.09 mg·h^{-1}·mg$_{Fe}^{-1}$/11.8%@−0.4 V) [42].

It is worth noting that the feeding N_2 was strictly purified prior to
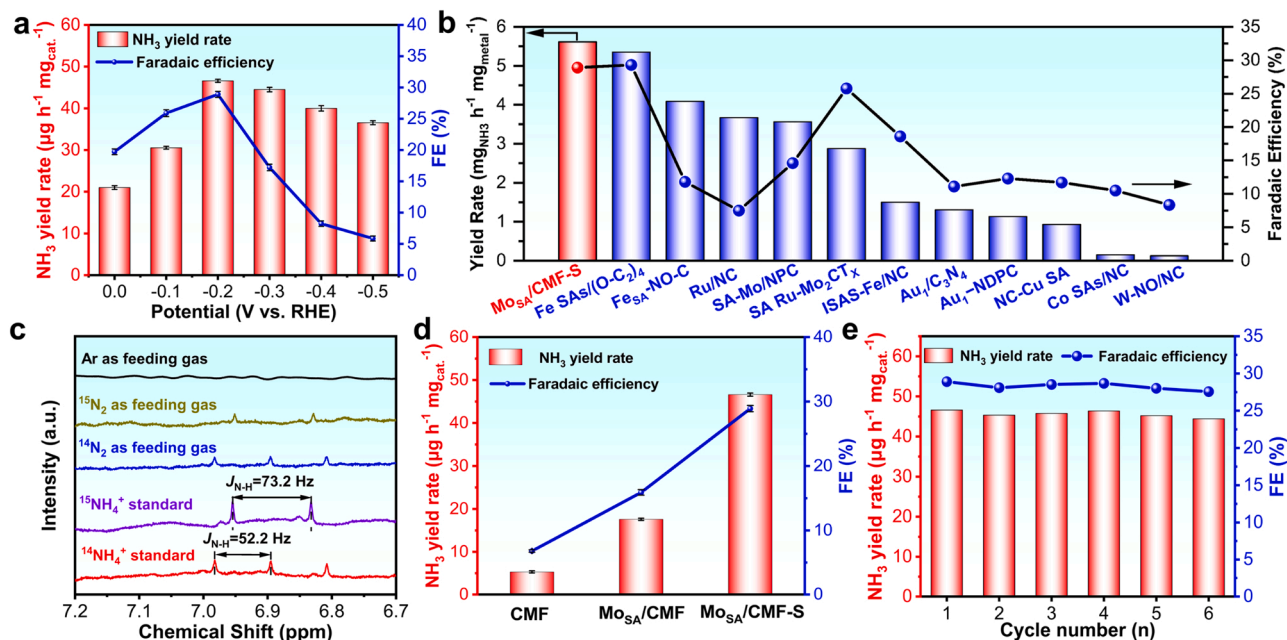
Fig. 3. Electrochemical NRR performance. (a) The NH_3 yield rates and Faradaic efficiencies of Mo_{SA}/CMF-S at different potentials for 2 h. (b) The optimal yield rate and FE of Mo_{SA}/CMF-S compared to various state-of-the-art SACs reported previously. Here, the NH_3 yield rates are normalized by dividing the corresponding active metal mass. (c) ^1H nuclear magnetic resonance spectra on Mo_{SA}/CMF-S at − 0.2 V vs RHE for 2 h using Ar, $^{14}N_2$ and $^{15}N_2$ as feeding gases, respectively, and corresponding $^{14}NH_4^+$ and $^{15}NH_4^+$ standard samples. (d) The optimal NH_3 yield rates and Faradaic efficiencies for Mo_{SA}/CMF-S, Mo_{SA}/CMF and CMF at − 0.2 V vs. RHE. (e) NH_3 yield rates and Faradaic efficiencies of Mo_{SA}/CMF-S at − 0.2 V during 6 cycling tests.

each NRR test to eliminate NO_x and N-containing species. The HCl electrolyte and N_2-fed electrolyte show no NH_3 or NO_x signals, ruling out the possibility of environmental interference with NH_3 production (Fig. S22 and S23). Furthermore, the UV–vis analysis in an Ar-saturated solution, blank solution, at open circuit, or on pristine carbon paper does not produce a detectable amount of NH_3 (Fig. S24a). On the contrary, the NH_3 only produced when the N_2 involved in the electrolyte. Additionally, a N_2-Ar gas switching experiments also showed that significant NH_3 yields were detected only in N_2-saturated solutions, but not in Ar-saturated solutions (Fig. S24b), substantially proved that the detected ammonia nitrogen source is generated by N_2 reduction, not the nitrogen atom of Mo_{SA}/CMF-S. Moreover, the linear increase in the total nitrogen in the ammonia produced with electrolysis time is clearly shown in Fig. S25. Meanwhile, the total nitrogen in the ammonia produced for 12 h (87.78 µg) is ≈ 14 times higher than that of the Mo_{SA}/CMF-S loaded on the carbon paper (6.32 µg), indicating that the NH_3 originates from the N_2 reduction instead of the catalyst. To directly identify the reliability, $^{15}N_2$ (99 atom%) isotopic labeling experiments were conducted. After 2 h of NRR electrolysis, the electrolytes saturated by different gases were detected by ^1H nuclear magnetic resonance. As shown in Fig. 3c, when using Ar as the feed gas, no specific chemical shift can be identified. However, when $^{14}N_2$ was supplied, the characteristic triplet peaks corresponded to the $^{14}NH_4^+$ standard ($^1J_{N-H}$ = 52.2 Hz). Furthermore, when $^{15}N_2$ was used instead of $^{14}N_2$, a double peak coupling peak of $^{15}NH_4^+$ ($^1J_{N-H}$ = 72.2 Hz) was found [44], substantially proved that feeding N_2 is the sole source of NH_3 generated in the NRR process. All these experiments unequivocally provide sufficient evidence that the nitrogen source of ammonia produced is only from N_2 reduction, not Mo_{SA}/CMF-S or others.

To elucidate the source of the superior NRR performance of Mo_{SA}/CMF-S, we performed NRR tests on Mo_{SA}/CMF and CMF for comparison (Fig. S26 and S27). Both of them exhibit similar yield and Faradaic efficiencies trends to Mo_{SA}/CMF-S at given potentials, reaching maximum values at − 0.2 V vs. RHE. Nevertheless, the two catalysts exhibited much lower NH_3 yield rates (Mo_{SA}/CMF: 17.6 µg·h^{-1}·mg_{cat}^{-1}, CMF: 5.3 µg·h^{-1}·mg_{cat}^{-1}) and Faradaic efficiencies (Mo_{SA}/CMF: 15.9%, CMF:

6.8%) than those of Mo_{SA}/CMF-S in Fig. 3d. The N_2 temperature-programmed desorption (N_2-TPD) curves for Mo_{SA}/CMF and Mo_{SA}/CMF-S. Both Mo_{SA}/CMF and Mo_{SA}/CMF-S exhibit a peak at approximately 90 °C, which was assigned to the physical adsorption signal of N_2 on catalysts (Fig. S28). Additionally, the desorption peak for Mo_{SA}/CMF-S was located at 479.0 °C, which was attributed to the chemical adsorption of N_2 on Mo species. In contrast, the chemical absorption peak of Mo_{SA}/CMF was at 366.8 °C, suggesting that the binding strength of N_2 on Mo_{SA}/CMF-S was much stronger than that on Mo_{SA}/CMF [47]. Therefore, due to the increased bonding strength with N_2, the doping of S can enhance the catalytic performance of a single Mo atom. Other evidence has also been explored for the effect of S on catalytic performance. Fig. S29 shows the LSV curves of the Mo_{SA}/CMF and Mo_{SA}/CMF-S catalysts in an Ar-saturated 0.1 M HCl solution. It exhibits that the current density of Mo_{SA}/CMF is higher than that of Mo_{SA}/CMF-S, indicating that Mo_{SA}/CMF-S possesses a poor HER activity [48]. Moreover, this result also indicates that doped S can significantly suppress the HER process, which will benefit the NRR reaction. This performance gap was also further identified through HER selectivity assessment. The H_2 selectivity of Mo_{SA}/CMF-S is lower than that of Mo_{SA}/CMF and CMF (Fig. S30), indicating that N_2 adsorption has a higher selectivity than H adsorption. On the other hand, Mo_{SA}/CMF-S possesses the highest capacitance of 7.49 mF cm^{-2}, indicating more exposed active sites from Mo_{SA}/CMF-S for catalyzing NRR (Fig. S31). The electrical impedance spectroscopic measurements (Fig. S32) reveal a more efficient electron transfer for Mo_{SA}/CMF-S than Mo_{SA}/CMF and CMF. Based on the above analyses, atomically dispersed Mo sites can efficiently catalyze NRR, as predicted by theoretical studies; the incorporation of S into the carbon matrix can largely suppress the competing HER by redistributing the electronic structure and thus boost the NRR selectivity of single Mo atoms.

Besides activity and selectivity, stability is also another critical feature of electrocatalysts. As shown in Fig. 3e, Mo_{SA}/CMF-S exhibits negligible decay in both NH_3 yield rate and FE during 6 successive NRR cycles, maintaining more than 95% of the initial values (44.4 µg·h^{-1}·mg_{cat}^{-1}/27.6%). Moreover, there was no loss in current

density after the chronoamperometry operation for 20 h (Fig. S33), followed by a slight decrease in the activity and selectivity, further demonstrating the robust stability of Mo$_{SA}$/CMF-S. To further reveal the stable feature, we conducted detailed characterizations of Mo$_{SA}$/CMF-S after NRR operation. The XRD pattern and high-resolution XPS spectra (Fig. S34) confirm the stability of the structure and composition. The samples have no difference before and after the NRR experiments. In addition, the electron microscopy (Fig. S35) images provide direct observations of the microstructures of the NRR sample. There is no obvious change or morphology or atom arrangement during NRR. Additionally, before and after the electrolysis, the contents of Mo, N and S remained almost identical to those of the original catalyst (Table S6). All the above analyses have proven the excellent stability of Mo$_{SA}$/CMF-S.

3.3. DFT calculations

Density functional theory (DFT) were conducted to gain insight into the catalytic activities of Mo$_{SA}$/CMF-S. Based on above analyses and previous works [15,18], single Mo atoms are probably coordinated by one N atom and two C atoms (Mo$_1$N$_1$C$_2$) and anchored on a carbon matrix. Here, we define these S-doped samples as Mo$_1$N$_1$C$_2$-Sx (x = 1, 2, …, 7). Firstly, we calculated the total energies for the Mo$_1$N$_1$C$_2$-Sx

species (Table S7). It is found that Mo$_1$N$_1$C$_2$-S7 is the most stable structure, in which the Mo atom directly interact with the S atom. However, the experimental observations suggest that there exist no strong interactions between the Mo and S atoms. Moreover, the energies of Mo$_1$N$_1$C$_2$-S2, Mo$_1$N$_1$C$_2$-S3 and Mo$_1$N$_1$C$_2$-S4 structures are almost the same, which are only about 0.4 eV higher than that of Mo$_1$N$_1$C$_2$-S7. The DFT calculations of NRR on the Mo$_1$N$_1$C$_2$-S2 and Mo$_1$N$_1$C$_2$-S3 were also performed (Table S8). It is found that the NRR activities of Mo$_1$N$_1$C$_2$-S2 and Mo$_1$N$_1$C$_2$-S3 are poorer than that of Mo$_1$N$_1$C$_2$-S4, which is consist with the charge transfer analysis. The calculated energies indicate that the existences of all the four structures in experiments. Secondly, the Bader analysis reveals that the doping of S introduces dramatic charge redistributions to the Mo atom, as seen from the Mo charge variations in Fig. 4a. The charges (electrons) of Mo in all the S-doped samples increase inordinately except Mo$_1$N$_1$C$_2$-S5 compared to the undoped Mo$_1$N$_1$C$_2$, and the increased number of electrons of Mo in Mo$_1$N$_1$C$_2$-S4 is the largest (approximately 0.3 e). Finally, the contour plots of the charge density difference of Mo atoms in Mo$_1$N$_1$C$_2$ and Mo$_1$N$_1$C$_2$-S4 in Fig. 4b illustrate that charges accumulate between S and Mo when the corresponding C atoms are replaced by S, strongly suggesting that the electron structure of Mo could be modulated by the doped S. Additionally, the hydrogen adsorption energy on the surface of the Mo$_1$N$_1$C$_2$ and
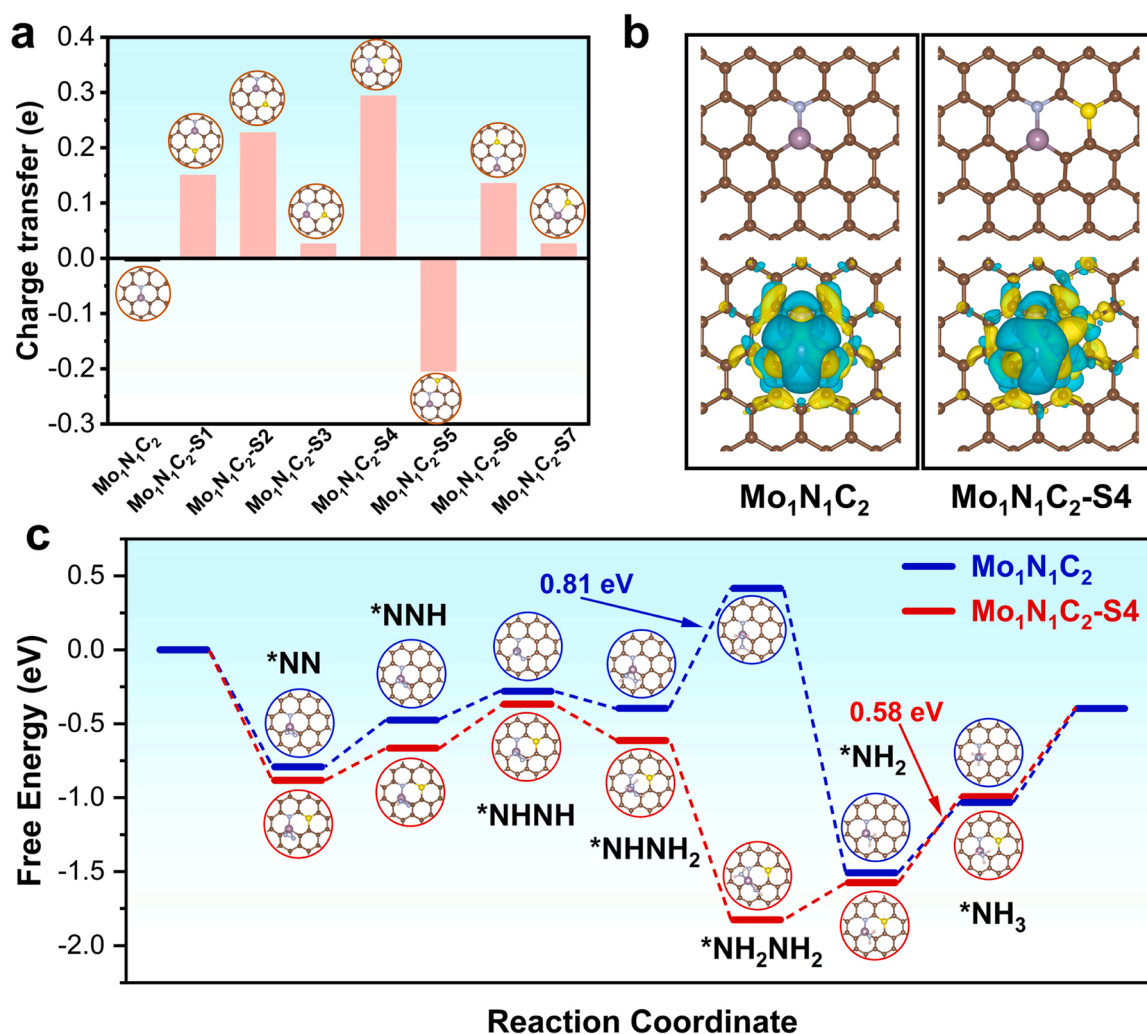

Fig. 4. Computational studies of electronic structure and reaction pathway. (a) Bader charge variations of the Mo atom in different S-doped samples with respect to the undoped sample. Insets illustrate the different structures of S-doped samples labeled by Mo$_1$N$_1$C$_2$-Sx with x = 1–7. (b) Optimized geometries and contour plots of the charge density differences for Mo$_1$N$_1$C$_2$ and Mo$_1$N$_1$C$_2$-S4. The accumulation and depletion of electrons on the models are highlighted by yellow and blue shads, respectively. (c) Diagrams of Gibbs free energy diagram of enzymatic NRR. The brown, gray, yellow, white and purple balls respectively present C, N, S, H and Mo atoms. The asterisk (*) illustrates a reactive intermediate adsorbed on a site in the model structure.

$Mo_1N_1C_2$-S4 samples was also calculated to evaluate the competing HER. It is obvious that the hydrogen adsorption free energy on $Mo_1N_1C_2$ is more conducive to hydrogen evolution than that on $Mo_1N_1C_2$-S4 (Fig. S36), indicating that the HER kinetics on the surface of $Mo_1N_1C_2$-S4 are sluggish [49]. Moreover, this result also suggests that doping S can significantly suppress the HER process, which is in good agreement with Fig. S29.

To elucidate the influences of electron redistribution of Mo atoms on the catalytic activity, the reaction free energy diagram of NRR on $Mo_1N_1C_2$ and $Mo_1N_1C_2$-S4 were mapped out. Generally, four mechanisms are considered for NRR: distal, alternating, enzymatic and consecutive paths. The adsorption energies are calculated to be -0.87 and -0.82 eV for the side-on and end-on patterns, respectively, revealing that the adsorbed N_2 prefers the side-on to the end-on configuration on a single Mo atom, which is consistent with previous research [50]. Accordingly, the Gibbs free energy diagram via the enzymatic and consecutive pathways is plotted in Fig. 4c, Fig. S37 and Table S9. Moreover, the correction of the ZPE and entropy of the NRR intermediates listed in the Table S10. Firstly, it is easy to find that $Mo_1N_1C_2$-S4 exhibits stronger binding with N_2 (-0.88 eV) than the undoped sample (-0.79 eV). Secondly, the potential-determining step (PDS) for $Mo_1N_1C_2$-S4 is a ΔG_{PDS} of 0.58 eV, which is lower than that on $Mo_1N_1C_2$ (0.81 eV) of the enzymatic pathway. Meanwhile, the ΔG_{PDS} for $Mo_1N_1C_2$-S4 of the consecutive pathway (0.70 eV) is also smaller than that of $Mo_1N_1C_2$ (0.74 eV). Finally, DFT calculations confirm that due to the synergy of enhancing N_2 adsorption and reducing ΔG_{PDS}, the doping of S can enhance the catalytic performance of a single Mo atom.

4. Conclusions

In summary, we have demonstrated that a single Mo atom supported on S-modified carbon multichannel fibers is highly efficient for the electroreduction of N_2 to NH_3 under ambient conditions. Detailed analyses demonstrate that the incorporated S atoms modulate the electron distribution of single Mo sites, which synergistically boost the adsorption/activation of N_2 and suppress the competitive HER. Meanwhile, the well-designed multichannel nanostructure endows the full accessibility of active sites and facilitates charge transfer. This catalyst affords a stable and record-high NH_3 yield rate of 5.61 mg·h^{-1}·mg$_{Mo}^{-1}$ and an FE of 28.9% at a low potential of -0.2 V vs. RHE in 0.1 M HCl. This work offers a prototype to synchronize the activity and selectivity of NRR electrocatalysts, which can generally be applied to other SACs for electrochemical applications beyond electrocatalysis.

CRediT authorship contribution statement

Lu Li: Conceptualization, Methodology, Data curation, Formal analysis, Writing – original draft. **Weikang Yu:** Methodology, Formal analysis, Data curation. **Wenbin Gong:** Software, Formal analysis, Data curation, Writing - original draft. **Hao Wang:** Conceptualization, Project administration, Formal analysis, Writing – original draft, Writing – review & editing, Supervision. **Chao-Lung Chiang:** Software, Formal analysis, Data curation. **Yanping Lin:** Formal analysis. **Jie Zhao:** Formal analysis, Supervision. **Labao Zhang:** Investigation, Supervision, Writing – review & editing. **Jong-Min Lee:** Investigation, Supervision, Writing – review & editing. **Guifu Zou:** Project administration, Supervision, Writing – review & editing, Supervision, Funding acquisition. All authors reviewed and commented on the manuscript before publication.

Declaration of Competing Interest

The authors declare that they have no known competing financial interests or personal relationships that could have appeared to influence the work reported in this paper.

Appendix A. Supporting information

Supplementary data associated with this article can be found in the online version at doi:10.1016/j.apcatb.2022.122038.

References

[1] B.H.R. Suryanto, H.L. Du, D.B. Wang, J. Chen, A.N. Simonov, D.R. MacFarlane, Challenges and prospects in the catalysis of electroreduction of nitrogen to ammonia, Nat. Catal. 2 (2019) 290–296.

[2] H.S. Kim, J. Choi, J. Kong, H. Kim, S.J. Yoo, H.S. Park, Regenerative electrocatalytic redox cycle of copper sulfide for sustainable NH_3 production under ambient conditions, ACS Catal. 11 (2021) 435–445.

[3] G. Qing, R. Ghazfar, S.T. Jackowski, F. Habibzadeh, M.M. Ashtiani, C.P. Chen, M. R. Smith, T.W. Hamann, Recent advances and challenges of electrocatalytic N_2 reduction to ammonia, Chem. Rev. 120 (2020) 5437–5516.

[4] Y.C. Wan, J.C. Xu, R.T. Lv, Heterogeneous electrocatalysts design for nitrogen reduction reaction under ambient conditions, Mater. Today 27 (2019) 69–90.

[5] X. Yan, D.L. Liu, H.H. Cao, F. Hou, J. Liang, S.X. Dou, Nitrogen reduction to ammonia on atomic-scale active sites under mild conditions, Small, Methods 3 (2019) 1800501.

[6] J. Li, M.F. Stephanopoulos, Y.N. Xia, Introduction: heterogeneous single-atom catalysis, Chem. Rev. 120 (2020) 11699–11702.

[7] S. Zhang, S.H. Lu, P. Zhang, J.X. Tian, L. Shi, C.Y. Ling, Q.H. Zhou, J.L. Wang, Accelerated discovery of single-atom catalysts for nitrogen fixation via machine learning, Energy Environ. Mater. (2022), https://doi.org/10.1002/eem2.12304).

[8] L.L. Han, X.J. Liu, J.P. Chen, R.Q. Lin, H.X. Liu, F. Lu, S. Bak, Z.X. Liang, S.Z. Zhao, E. Stavitski, J. Luo, R.R. Adzic, H.L.L. Xin, Atomically dispersed molybdenum catalysts for efficient ambient nitrogen fixation, Angew. Chem. Int. Ed. 58 (2019) 2321–2325.

[9] W. Peng, M. Luo, X.D. Xu, K. Jiang, M. Peng, D.C. Chen, T.S. Chan, Y.W. Tan, Spontaneous atomic ruthenium doping in Mo_2CT_X MXene defects enhances electrocatalytic activity for the nitrogen reduction reaction, Adv. Energy Mater. 10 (2020) 2001364.

[10] H.C. Tao, C. Choi, L.X. Ding, Z. Jiang, Z.S. Hang, M.W. Jia, Q. Fan, Y.N. Gao, H. H. Wang, A.W. Robertson, S. Hong, Y.S. Jung, S.Z. Liu, Z.Y. Sun, Nitrogen fixation by Ru single-atom electrocatalytic reduction, Chem 5 (2019) 204–214.

[11] C.Y. Ling, Y.X. Ouyang, Q. Li, X.W. Bai, X. Mao, A.J. Du, J.L. Wang, A general two-step strategy-based high-throughput screening of single atom catalysts for nitrogen fixation, Small, Methods 3 (2019) 1800376.

[12] X.Q. Wang, W.Y. Wang, M. Qiao, G. Wu, W.X. Chen, T.W. Yuan, Q. Xu, M. Chen, Y. Zhang, X. Wang, J. Wang, J.J. Ge, X. Hong, Y.F. Li, Y. Wu, Y.D. Li, Atomically dispersed Au_1 catalyst towards efficient electrochemical synthesis of ammonia, Sci. Bull. 63 (2018) 1246–1253.

[13] W.J. Zang, T. Yang, H.Y. Zou, S.B. Xi, H. Zhang, X.M. Liu, Z.K. Kou, Y.H. Du, Y. P. Feng, L. Shen, L.L. Duan, J. Wang, S.J. Pennycook, Copper single atoms anchored in porous nitrogen-doped carbon as efficient pH-universal catalysts for the nitrogen reduction reaction, ACS Catal. 9 (2019) 10166–10173.

[14] S.Y. Wang, L. Shi, X.W. Bai, Q. Li, C.Y. Ling, J.L. Wang, Highly efficient photo-/ electrocatalytic reduction of nitrogen into ammonia by dual-metal Sites, ACS Cent. Sci. 6 (2020) 1762–1771.

[15] Y.Y. Ma, T. Yang, H.Y. Zou, W.J. Zang, Z.K. Kou, L. Mao, Y.P. Feng, L. Shen, S. J. Pennycook, L.L. Duan, X. Li, J. Wang, Synergizing Mo single atoms and Mo_2C nanoparticles on CNTs synchronizes selectivity and activity of electrocatalytic N_2 reduction to ammonia, Adv. Mater. 32 (2020) 2002177.

[16] J.X. Zhao, Z.F. Chen, Single Mo atom supported on defective boron nitride monolayer as an efficient electrocatalyst for nitrogen fixation: a computational study, J. Am. Chem. Soc. 139 (2017) 12480–12487.

[17] W.H. Zhao, L.F. Zhang, Q.Q. Luo, Z.P. Hu, W.H. Zhang, S. Smith, J.L. Yang, Single Mo$_1$(Cr$_1$) atom on nitrogen-doped graphene enables highly selective electroreduction of nitrogen into ammonia, ACS Catal. 9 (2019) 3419–3425.

[18] W.X. Chen, J.J. Pei, C.T. He, J.W. Wan, H.L. Ren, Y.Q. Zhu, Y. Wang, J.C. Dong, S. B. Tian, W.C. Cheong, S.Q. Lu, L.R. Zheng, X.S. Zheng, W.S. Yan, Z.B. Zhuang, C. Chen, Q. Peng, D.S. Wang, Y.D. Li, Rational design of single molybdenum atoms anchored on N-doped carbon for effective hydrogen evolution reaction, Angew. Chem. Int. Ed. 56 (2017) 16086–16090.

[19] J.S. Lee, W. Kim, J. Jang, A. Manthiram, Sulfur-embedded activated multichannel carbon nanofiber composites for long-life, high-rate lithium-sulfur batteries, Adv. Energy Mater. 7 (2017) 1601943.

[20] H. Wang, Q.H. Yi, L.J. Gao, Y.Q. Gao, T.T. Liu, Y.B. Jiang, Y.H. Sun, G.F. Zou, Hierarchically interconnected nitrogen-doped carbon nanosheets for an efficient hydrogen evolution reaction, Nanoscale 9 (2017) 16342–16348.

[21] Y.Y. Tong, H.P. Guo, D.L. Liu, X. Yan, P.P. Su, J. Liang, S. Zhou, J. Liu, G.Q. Lu, S. X. Dou, Vacancy engineering of iron-doped W$_{18}$O$_{49}$ nanoreactors for low-barrier electrochemical nitrogen reduction, Angew. Chem. Int. Ed. 59 (2020) 7356–7361.

[22] C.L. Wang, D.D. Wang, S. Liu, P. Jiang, Z.Y. Lin, P.P. Xu, K. Yang, J. Lu, H.G. Tong, L. Hu, W.J. Zhang, Q.W. Chen, Engineering the coordination environment enables molybdenum single-atom catalyst for efficient oxygen reduction reaction, J. Catal. 389 (2020) 150–156.

[23] Q.H. Li, W.X. Chen, H. Xiao, Y. Gong, Z. Li, L.R. Zheng, X.S. Zheng, W.S. Yan, W. C. Cheong, R.A. Shen, N.H. Fu, L. Gu, Z.B. Zhuang, C. Chen, D.S. Wang, Q. Peng, J. Li, Y.D. Li, Fe isolated single atoms on S, N codoped carbon by copolymer pyrolysis strategy for highly efficient oxygen reduction reaction, Adv. Mater. 30 (2018) 1800588.

[24] J. Wang, H. Huang, P. Wang, S. Wang, J.P. Li, N, S synergistic effect in hierarchical porous carbon for enhanced NRR performance, Carbon 179 (2021) 358–364.

[25] Y.K. Wen, H. Zhu, J.C. Hao, S.L. Lu, W. Zong, F.L. Lai, P.M. Ma, W.F. Dong, T. X. Liu, M.L. Du, Metal-free boron and sulphur co-doped carbon nanofibers with optimized p-band centers for highly efficient nitrogen electroreduction to ammonia, Appl. Catal. B Environ. 292 (2021), 120144.

[26] J.Q. Zhang, Y.F. Zhao, C. Chen, Y.C. Huang, C.L. Dong, C.J. Chen, R.S. Liu, C. Y. Wang, K. Yan, Y.D. Li, G.X. Wang, Tuning the coordination environment in single-atom catalysts to achieve highly efficient oxygen reduction reactions, J. Am. Chem. Soc. 141 (2019) 20118–20126.

[27] L.B. Fan, Q. Li, D.W. Wang, T. Meng, M.X. Yan, Z.C. Xing, E.K. Wang, X.R. Yang, Electrospun Ru-RuO$_2$/MoO$_3$ carbon nanorods with multi-active components: a Pt-like catalyst for the hydrogen evolution reaction, Chem. Commun. 56 (2020) 739–742.

[28] Q.H. Li, W.X. Chen, H. Xiao, Y. Gong, Z. Li, L.R. Zheng, X.S. Zheng, W.S. Yan, W. C. Cheong, R.A. Shen, N.H. Fu, L. Gu, Z.B. Zhuang, C. Chen, D.S. Wang, Q. Peng, J. Li, Y.D. Li, Fe isolated single atoms on S, N codoped carbon by copolymer pyrolysis strategy for highly efficient oxygen reduction reaction, Adv. Mater. 30 (2018) 1800588.

[29] D.H. Guo, R. Shibuya, C. Akiba, S. Saji, T. Kondo, J. Nakamura, Active sites of nitrogen-doped carbon materials for oxygen reduction reaction clarified using model catalysts, Science 351 (2016) 361–365.

[30] Y.Y. Chen, Y. Zhang, W.J. Jiang, X. Zhang, Z.H. Dai, L.J. Wan, J.S. Hu, Pomegranate-like N,P-doped Mo$_2$C@C nanospheres as highly active electrocatalysts for alkaline hydrogen evolution, ACS Nano 10 (2016) 8851–8860.

[31] J.Q. Feng, H.S. Gao, L.R. Zheng, Z.P. Chen, S.J. Zeng, C.Y. Jiang, H.F. Dong, L. C. Liu, S.J. Zhang, X.P. Zhang, A. Mn-N$_3$, single-atom catalyst embedded in graphitic carbon nitride for efficient CO$_2$ electroreduction, Nat. Commun. 11 (2020) 4341.

[32] Y. Jia, X.Y. Xiong, D.N. Wang, X.X. Duan, K. Sun, Y.J. Li, L.R. Zheng, W.F. Lin, M. D. Done, G.X. Zhang, W. Liu, X.M. Sun, Atomically dispersed Fe-N4 modified with

[33] Q. Zhang, B.X. Wang, S. Chen, S.Y. Zhang, J.M. Hong, S edge/center-selectively doped graphene oxide for bisphenol a electro-degradation: preparation, efficiency and mechanism, Chem. Eng. J. 420 (2021), 127669.

[34] C. Tang, Y. Jiao, B.Y. Shi, J.N. Liu, Z.H. Xie, X. Chen, Q. Zhang, S.Z. Qiao, Coordination tunes selectivity: two-electron oxygen reduction on high-loading molybdenum single-atom catalysts, Angew. Chem. Int. Ed. 59 (2020) 9171–9176.

[35] K. Ba, G.L. Wang, T. Ye, X.R. Wang, Y.Y. Sun, H.Q. Liu, A.Q. Hu, Z.Y. Li, Z.Z. Sun, Single faceted two-dimensional Mo$_2$C electrocatalyst for highly efficient nitrogen fixation, ACS Catal. 10 (2020) 7864–7870.

[36] W.C. Xu, G.L. Fan, J.L. Chen, J.H. Li, L. Zhang, S.L. Zhu, X.C. Su, F.Y. Cheng, J. Chen, Nanoporous palladium hydride for electrocatalytic N$_2$ reduction under ambient conditions, Angew. Chem. Int. Ed. 59 (2020) 3511–3516.

[37] P.L. Searle, The berthelot or indophenol reaction and its use in the analytical chemistry of nitrogen, Analyst 109 (1984) 549–568.

[38] G.W. Watt, J.D. Chrisp, A spectrophotometric method for determination of hydrazine, Anal. Chem. 24 (1952) 2006–2008.

[39] S.S. Liu, M.F. Wang, T. Qian, H.Q. Ji, J. Liu, C.L. Yan, Facilitating nitrogen accessibility to boron-rich covalent organic frameworks via electrochemical excitation for efficient nitrogen fixation, Nat. Commun. 10 (2019) 3898.

[40] Y. Gu, B.J. Xi, W.Z. Tian, H. Zhang, Q. Fu, S.L. Xiong, Boosting selective nitrogen reduction via geometric coordination engineering on single-tungsten-atom catalysts, Adv. Mater. 33 (2021) 2100429.

[41] H.C. Tao, C. Choi, L.X. Ding, Z. Jiang, Z.S. Hang, M.W. Jia, Q. Fan, Y.N. Gao, H. H. Wang, A.W. Robertson, S. Hong, Y.S. Jung, S.Z. Liu, Z.Y. Sun, Nitrogen fixation by Ru single-atom electrocatalytic reduction, Chem 5 (2019) 204–214.

[42] Y. Li, J.W. Li, J.H. Huang, J.X. Chen, Y. Kong, B. Yang, Z.J. Li, L.C. Lei, G.L. Chai, Z. H. Wen, L.M. Dai, Y. Hou, Boosting electroreduction kinetics of nitrogen to ammonia via tuning electron distribution of single-atomic iron sites, Angew. Chem. Int. Ed. 60 (2021) 9078–9085.

[43] Y.M. Liu, Q. Xu, X.F. Fan, X. Quan, Y. Su, S. Chen, H.T. Yu, Z.J. Cai, Electrochemical reduction of N$_2$ to ammonia on Co single atom embedded N-doped porous carbon under ambient conditions, J. Mater. Chem. A 7 (2019) 26358–26363.

[44] F. Lu, S.Z. Zhao, R.J. Guo, J. He, X.Y. Peng, H.H. Bao, J.T. Fu, L.L. Han, G.C. Qi, J. Luo, X.L. Tang, X.J. Liu, Nitrogen-coordinated single Fe sites for efficient electrocatalytic N$_2$ fixation in neutral media, Nano Energy 61 (2019) 420–427.

[45] Q. Qin, T. Heil, M. Antonietti, M. Oschatz, Single-site gold catalysts on hierarchical N-doped porous noble carbon for enhanced electrochemical reduction of nitrogen, Small, Methods 2 (2018) 1800202.

[46] S.B. Zhang, M. Jin, T.F. Shi, M.M. Han, Q. Sun, Y. Lin, Z.H. Ding, L.R. Zheng, G. Z. Wang, Y.X. Zhang, H.M. Zhang, H.J. Zhao, Electrocatalytically active Fe-(O-C$_2$)$_4$ single-atom sites for efficient reduction of nitrogen to ammonia, Angew. Chem. Int. Ed. 59 (2020) 13423–13429.

[47] C.Y. Yang, B.L. Huang, S.X. Bai, Y.G. Feng, Q. Shao, X.Q. Huang, A generalized surface chalcogenation strategy for boosting the electrochemical N$_2$ fixation of metal nanocrystals, Adv. Mater. 32 (2020) 2001267.

[48] J.C. Zhang, B. Zhao, W.K. Liang, G.S. Zhou, Z.Q. Liang, Y.W. Wang, J.Y. Qu, Y. H. Sun, L. Jiang, Three-phase electrolysis by gold nanoparticle on hydrophobic interface for enhanced electrochemical nitrogen reduction reaction, Adv. Sci. 7 (2020) 2002630.

[49] B. Yu, H. Li, J. White, S. Donne, J.B. Yi, S.B. Xi, Y. Fu, G. Henkelman, H. Yu, Z. L. Chen, T.Y. Ma, Tuning the catalytic preference of ruthenium catalysts for nitrogen reduction by atomic dispersion, Adv. Funct. Mater. 30 (2020) 1905665.

[50] Y. Ying, K. Fan, X. Luo, J. Qiao, H. Huang, Transition metal-tetracyanoquinodimethane monolayers as single-atom catalysts for the electrocatalytic nitrogen reduction reaction, Mater. Adv. 1 (2020) 1285–1292.